Original Article

Label-free molecular profiling for identification of biomarkers in carcinogenesis using multimodal multiphoton imaging

Yuan Liu[1,2], Haohua Tu[1], Sixian You[1,2], Eric J. Chaney[1], Marina Marjanovic[1,2], Stephen A. Boppart[1,2,3,4]

[1]Beckman Institute for Advanced Science and Technology, [2]Department of Bioengineering, [3]Department of Electrical and Computer Engineering, [4]Carle Illinois College of Medicine, University of Illinois at Urbana-Champaign, Urbana, IL, USA

Correspondence to: Stephen A. Boppart. Beckman Institute for Advanced Science and Technology, University of Illinois at Urbana-Champaign, 405 North Mathews Avenue, Urbana, Illinois 61801, USA. Email: boppart@illinois.edu.

Background: Label-free molecular profiling, imaging, and analysis are of particular interest in cancer biology for detecting subtle biochemical changes during cancer progression and potentially during cancer treatment. Multimodal, multiphoton imaging that combines diverse molecular contrasts derived from different physical mechanisms can improve our understanding of the tumor microenvironment.

Methods: A label-free optical molecular profiling technique has been developed based on penta-modal multiphoton imaging to investigate mammary tumor progression in a pre-clinical rat model. Pulses from a coherent supercontinuum were tailored for two-photon (2PF) and three-photon fluorescence (3PF), second (SHG) and third harmonic generation (THG), and hyperspectral coherent anti-Stokes Raman scattering (CARS)-based imaging. A graphic multiphoton molecular profiling model was constructed to intuitively combine the co-registered quantitative, chemical, functional, and structural tissue information, enabling longitudinal *in situ* biomolecular analysis.

Results: Over a 9-week period of tumor progression, and even before the formation of solid tumor, we observed lipid-protein transitions, microenvironmental reorganization, and a shift from FAD to NAD(P)H fluorescence, which reflects the reprogramming of cellular metabolism in carcinogenesis.

Conclusions: Multimodal multiphoton imaging reveals and interrelates diverse carcinogenic signatures, identifying biomarkers that could serve as early molecular indicators for breast cancer diagnosis. This quantitative multimodal imaging methodology for molecular profiling of associated cancer biomarkers may have a broader impact in fundamental cancer research and future clinical applications.

Keywords: Cancer biomarkers; mammary tumor; microenvironment; molecular profiling; multimodal multiphoton imaging; nonlinear optical imaging

Submitted Feb 25, 2019. Accepted for publication Apr 10, 2019.
doi: 10.21037/qims.2019.04.16
View this article at: http://dx.doi.org/10.21037/qims.2019.04.16

Introduction

Molecular imaging and profiling methods are not only important for cancer biology research, but also crucial for clinical diagnosis (1,2). In recent studies in mice, it was shown that metastasis may occur at early stages of carcinogenesis, not only at the later stages as previously thought (3,4). In addition, it is well documented that complex pathways of tumor progression strongly depend on the physical and molecular properties of the tumor microenvironment (5,6). These findings indicate the need for establishing reliable biomolecular markers for tumor progression.

While cancer cells and their microenvironment have been well defined using traditional histology and biochemical assays (6), label-free visualization and analysis of the biomolecular contents in our study offer

the capability to investigate carcinogenesis in the native tissue state, and has the potential for elucidating processes during early carcinogenesis for improving breast cancer detection and diagnosis (7). The most powerful aspect of multiphoton imaging is the diverse molecular contrasts that can be generated from various nonlinear optical events, in addition to other notable advantages of optical sectioning, deeper imaging penetration, and reduced absorption of longer wavelength light. Two-photon fluorescence (2PF) and three-photon fluorescence (3PF) microscopy enable imaging of endogenous fluorophores using a near-infrared laser (8,9). Second harmonic generation (SHG) and third harmonic generation (THG) imaging map optical non-centrosymmetry and heterogeneity derived from the second- and the third-order nonlinear susceptibilities, respectively (10,11). Coherent anti-Stokes Raman scattering (CARS) and stimulated Raman scattering (SRS) microscopy visualize the biochemical composition based on the intrinsic molecular vibrations (12,13). Note that in this paper, the coherent Raman response at xxxx cm^{-1} is abbreviated as Rxxxx.

In separate studies, label-free imaging of cellular species and collagen fibers in mouse mammary tumor was demonstrated by 2PF and SHG microscopy, respectively (14). The cellular FAD fluorescence and the collagen reorganization in the tumor microenvironment were also investigated by 2PF and SHG imaging (15,16). Metabolism of breast cancer cell lines indicated by FAD and NAD(P)H levels was studied by 2PF along with fluorescence lifetime imaging, and further characterized by an optical redox ratio (17-19). In addition, the functional roles of lipids in promoting tumor progression was examined by CARS microscopy (20,21), and molecularly-based breast cancer margin detection was realized by CARS spectroscopic imaging (22). While lipid boundaries and microvesicles can be probed by THG imaging, this modality has otherwise found limited applications in cancer research (23,24). In our more recent studies, it was successfully demonstrated that the co-registration of these modalities directly from fresh tissue offers various vital signatures in unperturbed physiological conditions (25-28). Building on these previous studies, the work presented here aims to utilize the comprehensiveness of the penta-modal quantitative imaging and to characterize changes observed longitudinally in carcinogenesis via graphical and quantitative analysis of the intrinsic chemical, metabolic, molecular, and structural information within the tumor microenvironment.

Label-free optical imaging combined with quantitative analysis could offer alternative insights into breast cancer detection and diagnosis, in parallel with conventional histopathology and biochemical assays (25-32). As each multiphoton modality targets a specific subset of biomolecules, these studies have focused on the molecular species detectable by the pre-determined optical setups (*Table S1*). A more comprehensive understanding of the relevant tumorigenic events, however, is limited, so the multimodal and spectral data were integrated and correlated to profile molecular changes and begin to elucidate the complex processes occurring during carcinogenesis. Based on the data from this longitudinal study of rat mammary tumor development, we present a novel approach for quantitatively and graphically profiling changes that occur in the tumor microenvironment during carcinogenesis.

Methods

Coherent supercontinuum (SC)

A Yb:KYW pulsed laser of 1,041-nm central wavelength, 220-fs pulse width (FWHM), and 80-MHz repetition rate (FemtoTRAIN IC, High Q Laser) was employed as the pump laser for coherent SC generation (*Figure S1*). The laser was coupled into a 21-cm segment of polarization-maintaining all-normal-dispersion nonlinear fiber (NL-1050-NEG-1-PM, NKT Photonics) by an aspheric lens (33). The pumping power was adjusted by a neutral density filter, and the laser polarization was aligned to the slow axis of the fiber by a half-wave plate. The output (input) coupling power was maintained at 480 (800) mW during all imaging sessions. The SC spectrum was recorded by an optical spectrum analyzer (*Figure S2*). The output SC was collimated by an off-axis parabolic mirror (Toptica Photonics) and guided into the imaging system. The parabolic mirror alignment was optimized by fine-tuning the beam shape at a distance longer than the system beam path by using a beam profiler (BGS-USB-SP620, Ophir-Spiricon).

Multiphoton imaging system

In the system, the wave-breaking band (780–880 nm) of the SC was reflected by a dichroic mirror (DMLP900, Thorlabs) (33), and the main SC (900–1,300 nm) was sent into a pulse shaper (MIIPSBox 640, Biophotonic Solutions). Blocks of 3" (4") SF57 glass were placed in the wave-breaking band (main-SC) beam for chirping the pulses,

and a motorized delay was installed in the main-SC path for tuning the vibrational frequency in spectral focusing CARS. The two beams were recombined by another identical dichroic, guided into a microscope modified from a commercially available frame (BX61WI, Olympus), and focused by a super-apochromat objective (UPLSAPO 60xW/IR, N.A. =1.20, Olympus). At the objective focus, the pulses were tailored for specific multiphoton imaging modalities, as will be discussed in the following section. Imaging was conducted by raster scanning a piezoelectric stage (P-575.3R7, PI). The pixel dwell time was 200 µs for all the imaging modalities. Starting in Week 6 of the longitudinal study, an additional 3PF image was acquired at a 1 ms pixel dwell time. All multiphoton signals were collected in an epi-geometry, passed through a selected filter on a filter wheel (*Table S2*), and detected by a photomultiplier tube (H7421-40, Hamamatsu).

Pulse shaping

For 2PF, SHG, 3PF, and THG imaging, pulses of selected spectral ranges were compressed to the transform-limit for selective and efficient imaging of endogenous molecules and structures (*Table S2*) (34,35). For 2PF, the 910–970 nm band was used to target FAD and elastin. For SHG and THG, the 1,140–1,200 nm band was used to minimize 2P excitation and to shift the emission closer to visible wavelengths with reduced optical loss and higher detection efficiency. SHG and THG were employed to image optical non-centrosymmetry and heterogeneity, respectively. For 3PF, the bands from 1,140–1,200 nm and 1,080–1,200 nm (additional imaging set starting in Week 6) were used to target NAD(P)H. The pulse shaper was utilized to spectrally select the spectral bands and to compensate the spectral phases measured at the objective focus (36,37). The amplitude and compensation phase masks were recorded and applied in the imaging sessions. For CARS, a spectral focusing technique was employed to spectrally concentrate the SC power into a single vibration (38). For imaging in the CH stretching region (2,800–3,200 cm^{-1}), the stokes beam of 1,030–1,215 nm was selected by amplitude shaping. An additional chirp of 4,500 fs^2 was introduced onto the Stokes beam by phase shaping for optimal performance of spectral focusing at this designated vibrational band, with a measured spectral resolution of 14 cm^{-1}. The amplitude and optimal phase mask were recorded and applied in the imaging sessions.

Multiphoton molecular profiles (MPMPs)

A MPMP was established, which constitutes a hexagonal radar plot of the signals collected from each co-registered set of pixels in each of the six collected images (2PF, SHG, 3PF, THG, R2850, R3050) (*Figure 1A*) and a hyperspectral CARS spectrum from the CH stretching region (2,800–3,200 cm^{-1}) (*Figure 1B*). The design of the radar plot directly reveals the lipid-protein transition, the optical structure, the metabolic activity, and their correlations. In addition, the CARS spectrum conveys the molecular vibrations, including CH_2 (R2850), CH_3 (R2930), =CH (R3015), CH aromatic (R3050), and OH stretching (>R3200) signatures in the CH stretching region (*Figure 1B*). The complimentary information fosters a further understanding of the spatially-resolved biomolecular composition in the tumor microenvironment, and how this changes over time, such as during carcinogenesis.

Opto-histology

The opto-histology, generated as a composite image using ImageJ (National Institutes of Health), comprises pseudo-colored multiphoton images (2PF-yellow, SHG-green, 3PF-cyan, THG-magenta, R2850-blue, R3050-red) to mimic conventional histopathological visualization. The composite is a result from the channel merging function (linear combination of all the pseudo-colored multiphoton channels) from ImageJ.

Animal study

The animal procedures for this study were conducted under a protocol approved by the Institutional Animal Care and Use Committee at the University of Illinois at Urbana-Champaign. A total of 18 female rats (F344, Harlan, 7-weeks old at the beginning of the experiment) were included in the study, with 9 cancer-induced and 9 control animals. Mammary tumors were induced by intraperitoneal injection of N-nitroso-N-methylurea (MNU, Sigma) at a concentration of 55 mg/kg (39). For the control animals, any effect caused by the injection was accounted for by injection of an identical quantity of saline. Two injections, one week apart, were administered, with the first injection on the left side and the second on the right side of abdomen. MNU-induced rat mammary tumor model was used in this study because the anatomical and pathological features, the hormone dependency, and the immunohistochemical

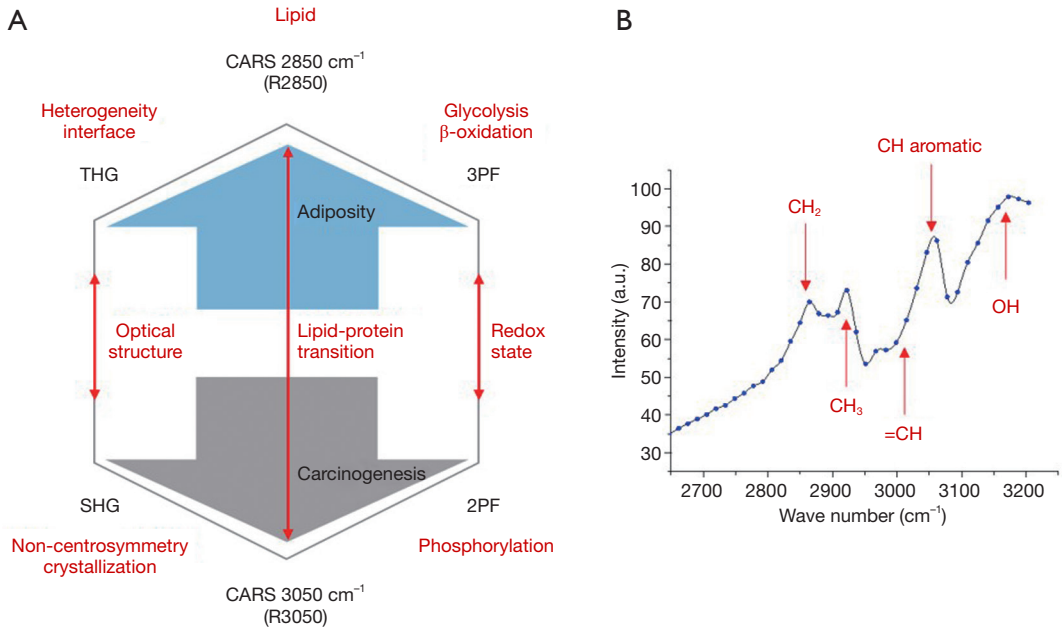

Figure 1 Molecular profiling based on multimodal multiphoton imaging. (A) Design of the hexagonal radar plot of the multiphoton molecular profile depicting the lipid-protein transition, the optical structures, and the metabolic activities in the tumor microenvironments. The blue and grey arrows provide a general guidance for adiposity and carcinogenesis, respectively. (B) A CARS spectrum in the CH stretching region and the important Raman shifts are indicated. The CH_2 (R2850) and CH aromatic (R3050) bands indicate the lipid and the protein compositions, respectively.

responses of the lesions all mimic human ductal carcinoma *in situ* (DCIS) (39-42).

One cancer-induced animal and one control animal were sacrificed each week. The mammary glands were excised, transferred into a Petri dish with saline, and stored in a refrigerator at 4 ℃. The imaging sessions were conducted within 6 hours of tissue resection. The tumor developmental status was assessed by an experienced biologist during the surgery and categorized into five stages as (I) normal: white and thin mammary gland; (II) suspicious: slightly darker mammary gland; (III) developing tumor: tumor masses <1 mm in diameter, orange-color granular formation; (IV) tumorous: tumors 1–3 mm in diameter, multiple granular features; (V) necrotic: tumors 3–10 mm in diameter, with necrotic cores. In the cancer-induced animals, the imaging sites were selected from the (pre-)tumorous regions in order to capture the molecular changes in the developing tumor. In the control animals, the imaging sites were chosen to approximate the corresponding regions of the mammary glands at which the cancer-induced animals were imaged. For each animal, 3–5 sites were imaged, and representative images from the longitudinal database are presented here.

Immediately after the imaging, mammary tissue specimens were placed in formalin and later processed for standard hematoxylin and eosin (H&E)-stained histology.

Results

Visualization of MPMPs by hexagonal radar plots

Penta-modal multiphoton imaging, including 2PF, SHG, 3PF, THG, and hyperspectral CARS, was enabled by shaping pulses from a coherent SC, which was generated by pumping an all-normal-dispersion fiber using a pulsed laser, producing a spectrum spanning the optical biological window of 780–1,300 nm (43). For 2PF, SHG, 3PF, and THG, the SC pulses were spectrally filtered by amplitude shaping and compressed to the transform-limit by phase shaping for selective and efficient imaging (34,35). For CARS, the SC pulses were also spectrally filtered but optimally chirped for spectral focusing in the CH stretching region. The complimentary molecular imaging capabilities visualized diverse biomolecules and structures in the same mammary tumor microenvironments and were employed to investigate mammary tumor development in a carcinogen-

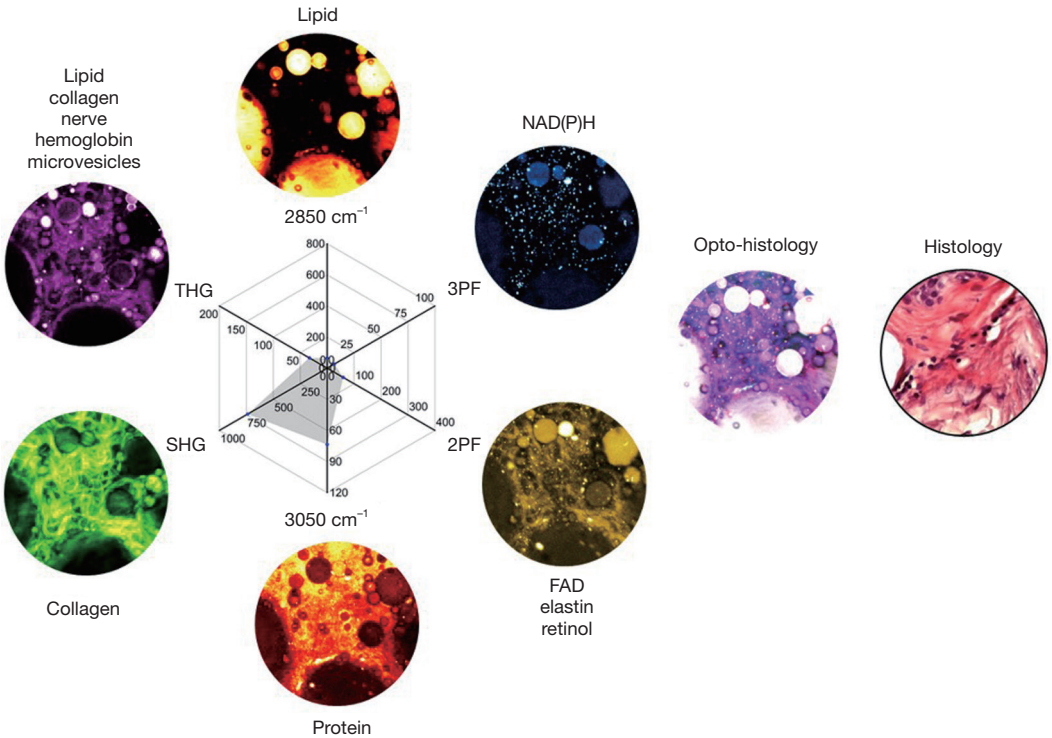

Figure 2 Multiphoton molecular profiling of tissue. Correlation of multiphoton signals and their represented structures. On the left (clockwise from top): CARS 2,850 cm^{-1}, 3PF, 2PF, CARS 3,050 cm^{-1}, SHG, THG images. On the right: pseudo-colored opto-histology image generated from a linear combination of the six modality images, along with a corresponding histology image of the same site. Image diameter: 175 μm.

induced rat model through a 9-week longitudinal study. MPMPs were developed to analyze the biomolecular content *in situ*, consisting of a hexagonal radar plot of the optical signals of 2PF, SHG, 3PF, THG, R2850, and R3050, along with the CARS spectrum (*Figure 2*). The correlation of the multiphoton and the vibrational responses allows for direct interrogation of lipid-protein transitions, along with optical structures, metabolic activity, and their relevance during tumor progression, facilitating the identification of new optical cancer biomarkers.

Multimodal multiphoton imaging of mammary tumor microenvironments

Various tumorigenic signatures revealed by multimodal multiphoton imaging and molecular profiling are demonstrated by large-area imaging in Week 8 of the carcinogen-induced mammary tumor and described in this section. At a tumor-stroma boundary (*Figure 3A*), abundant tumor cells (T: 2PF, 3PF, THG, R2850, R3050) are enclosed by the straightened collagen fibers (red arrow: SHG) assigned as the tumor-associated collagen signatures-2 (TACS-2) (15,16,29). The stromal cells (Ce: 2PF), which resemble tumorigenic epithelial cells and fibroblasts (44), show mostly FAD-fluorescence, marking their metabolic difference from tumor cells. The tumor-associated THG-sensitive microvesicles (TATVs; Tv) are also found in the tumor nest (24), confirming the tumorigenic activities. The TACS-3 feature (yellow arrow: SHG) is recognized as the collagen fibers aligned perpendicular to the TACS-2 feature, facilitating tumor invasion (15,16). The local invasion is cross-validated by multimodal imaging. 2PF imaging demonstrates tumor cells forming a protrusion infiltrating into the stroma, while 3PF imaging exhibits aligned microvesicles in parallel to the TACS-3 feature. Based on the excitation and detection wavelengths (*Table S2*), these microvesicles likely possess elevated NAD(P)H levels related to angiogenesis (45,46), and are designated as angiogenesis-associated 3PF-sensitive microvesicles (AA3V; 3v). THG imaging displays the TATVs in the proximity of

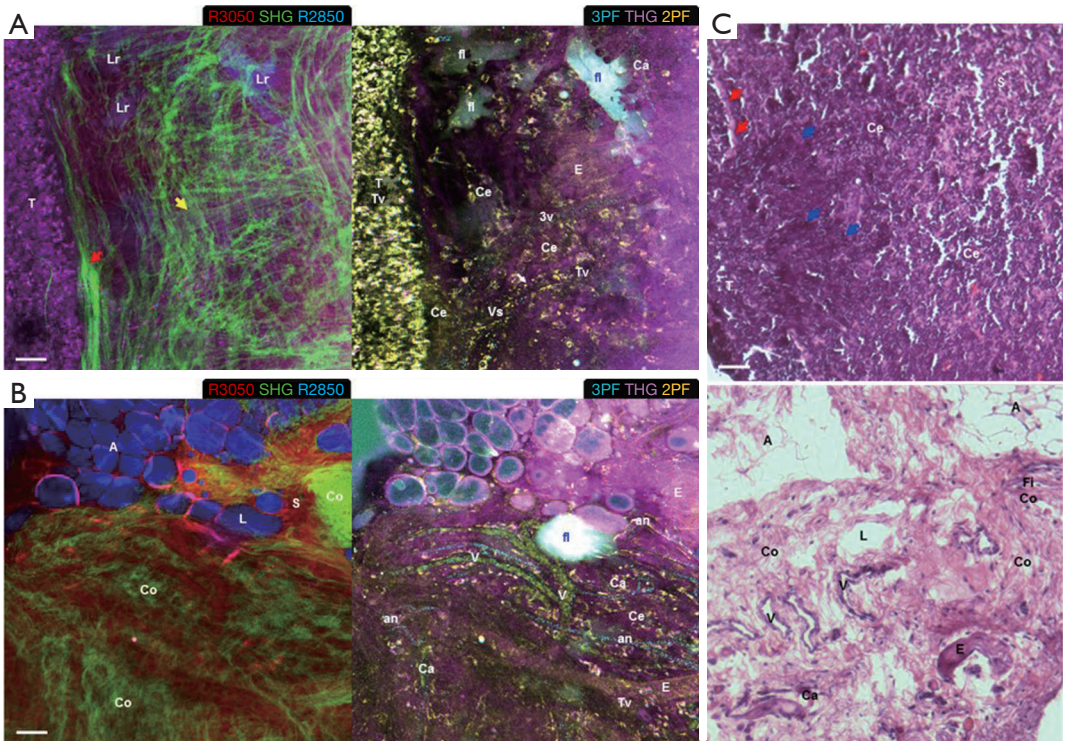

Figure 3 Multimodal multiphoton image of rat mammary tumor microenvironment. (A) A tumor-stroma boundary showing local invasion cross-validated by the distribution of FAD- and NAD(P)H-fluorescent cells, collagen and elastin organization, transmission of tumor-associated microvesicles, and lipid metabolism. (B) A lipid-stroma interface demonstrating diverse angiogenic features, lipid degradation and metabolism, and fibrocystic changes. Morphological features—A, adipose tissue; an, angiogenesis; Ca, capillary; Ce, hypercellularity; Co, collagen fiber; E, elastin fiber; Fi, fibroblast; fl, fluorescent feature; L, lipid droplet; Lr, lipid residue; S, stroma; T, tumor; Tv, THG-sensitive microvesicle; V, blood vessel; 3v, 3PF-sensitive microvesicle; red arrow, TACS-2 feature; yellow arrow, transmission of 3PF-sensitive vesicles along TACS-3 feature. Scale bar: 50 μm. (C) The corresponding H&E histology. Morphological features—A, adipose tissue; Ca, capillary; Ce, hypercellularity; Co, collagen fiber; E, elastin fiber; Fi, fibroblast; L, lipid droplet; T, tumor; V, blood vessel; red arrows, TACS-2 feature; blue arrows, cords of invading tumor cells. Scale bar: 50 μm.

the TACS-3 feature as well.

Several lipid residues (Lr: R2850) that are leftover lipid content from lipid degradation are found demonstrating high 2PF and 3PF, which reflects upregulated FAD and NAD(P)H levels due to the occurrence of β-oxidation (47). Near the lipid residues, a capillary (Ca: 2PF, 3PF) and an elastin net (E: 2PF) are identified, suggesting the relationship between lipolysis and angiogenesis. The lipid metabolism is likely fueling the angiogenesis while the neovascularization can potentially facilitate transportation of free fatty acids to promote tumor growth (20,21). The orientation of the elastin fibers is in concert with that of the collagen fibers and the microvesicles, and therefore potentially forming blood vessels in the same direction (48,49). The tumor cells (T) are marked with dense, dark-staining nuclei, while the surrounding connective tissue clearly defines a boundary (red arrows). Cords of malignant cells (blue arrows) are found infiltrating into the stroma.

In addition, a distinct set of tumorigenic signatures is identified at the interface of vascularized stroma and degraded adipose tissue (*Figure 3B*). Various angiogenic features are also seen, including blood vessels (V) with higher 2PF and less AA3Vs, capillaries (Ca) with similar characteristics but smaller in size, developing vasculature (an) with lower 2PF and more AA3Vs, and elastin fibers (E: 2PF) without AA3Vs (45,46,48,49). The stromal collagen fibers (Co: SHG, THG) present an inverse contrast to the high-2PF vasculature, suggesting the relevance of collagen remodeling and angiogenesis (15,16,48,49). The angiogenic site (an) on the right side of the image shows the elongated

high-2PF cells lining up with the AA3Vs. These FAD-fluorescent cells are likely tumor and endothelial cells participating in neo-vascularization. While there are no tubularly aligned FAD-fluorescent cells in the absence of AA3Vs, one can conclude that the AA3Vs may be capable of recruiting these cells in angiogenesis.

The degraded adipose tissue (A: R2850, THG, 3PF) possesses loosely attached lipid droplets (LDs; L: R2850, THG, 3PF), and some LDs lose their typical round shape and appear to be dispersed into the stroma forming lipid deposits. The lack of collagen fibers and the presence of empty spaces nearby relate the loss of the connective tissue to the degradation of adipose tissue. In the area surrounding the lipid deposits, near the center of the image, there exists an amorphous highly-fluorescent feature (fl), demonstrating high 3PF and moderate 2PF and THG signals. The upregulated 3PF indicates the higher NAD(P)H levels from β-oxidation (47), and the proximity to the vasculature again links lipid metabolism to angiogenesis. In the top-right corner of the image (*Figure 3B*), an abnormal collagen aggregate (Co: SHG, THG), designated as a TACS-1 feature of locally dense collagen (15,16) with elastin fibers within (E: 2PF), is identified as fibrocystic change (31).

In the corresponding H&E histology (*Figure 3C*), the elongated dark-staining lumens and connective tissue are developing vasculature (V) and elastin fibers (E), respectively. The adipose tissue (A) is disrupted during histological processing, but the LDs within the connective tissue (L) leave an empty space, which is clearly discernable. The collagenous connective tissue (Co) reflects different arrangements, but a sphere-like organization with fibroblasts (Fi) within corresponds to the fibrocystic tissue.

Multiphoton molecular profiling for mammary tumor development

Mammary tissue was dissected and imaged each week after the injections, but only selected data are presented to highlight the progression of findings.

The large-area multimodal imaging of the normal tissue in the control group (*Figure 4*) displays normal adipose tissue from the mammary gland (A: R2850, THG, 3PF), with little stromal connective tissue (R3050) and collagen fibers (Co: SHG) within.

During early-state tumor development (Week 1) in a carcinogen-injected rat, no tumor was palpable or visually identified, and the mammary gland was observed to be visually normal. However, in the multiphoton image (*Figure 5*), an FAD-fluorescent cell cluster (Ce: 2PF) is surrounded by dense collagen fibers (Co: SHG) extending outward. A mammary duct (D) is found with high 2PF, 3PF, THG, and R2850 signals (30). Within the cell cluster, Area 1 shows an MPMP (*Figure 5B*) of strong 2PF and R3050 responses, and a protein-like CARS spectrum marked with CH_2 stretching at R2930, CH aromatic stretching at R3050, and the co-existing water OH stretching at >R3200, while Area 2 demonstrates higher THG and 2PF. Some small LDs (R2850, THG) are identified near the cell cluster. Among them, Area 3 displays an MPMP with slightly higher THG and lower 2PF signals as compared to Area 2. Its CARS spectrum shows a lipid-like feature with CH_3 stretching at R2850, but also the above-mentioned protein-like features.

In Week 4 of tumor progression, suspicious sites were recognized as slightly darker regions in the mammary tissue. Multiphoton imaging (*Figure 6*) readily reveals highly-fluorescent tumor cells (T: 2PF, 3PF), reduced collagen content (SHG), and TATVs. In a void-line area (Area 1), the MPMP shows low multiphoton responses from all the modalities but still a protein-like spectrum. Area 2 targets a cluster of TATVs within a FAD-fluorescent cell, showing intense THG and strong 3PF. The higher 2PF and 3PF indicate higher cellular FAD and NAD(P)H levels, likely due to the interaction of the TATVs and the tumor cells. Similarly, the TATV outside the cells in Area 3 was analyzed, and its MPMP also demonstrates prominent THG but lower 2PF and 3PF. This comparison directly differentiates the free TATVs from those interacting with the tumor cells and relates TATVs to increased cellular metabolism.

In Week 6, a developing tumor mass (<1 mm) was identified during the animal surgery. Multiphoton imaging (*Figure 7*) shows several new tumorigenic signatures at a lipid-stroma boundary, including highly-fluorescent stromal cells (Ce: 2PF, 3PF), TATVs (Tv) in the stroma and near the LDs, and AA3Vs (3v) in a tubular arrangement in the vicinity of the developing blood vessel (an). Selected microvesicles are analyzed by MPMP. Area 1 (*Figure 7B*) demonstrates an MPMP with intense THG, moderate 3PF and 2PF, and a protein-like CARS spectrum, and therefore can be designated as a TATV. Area 2 exhibits extreme 3PF and R3050, intense 2PF, and a CARS spectrum with R2850 higher than R2930, as well as a R3050 vibration. The 2PF and 3PF responses convey the elevated FAD and NAD(P)H levels from the associated metabolic activities. A 3PF-sensitive microvesicle in Area 3 near the adipose tissue

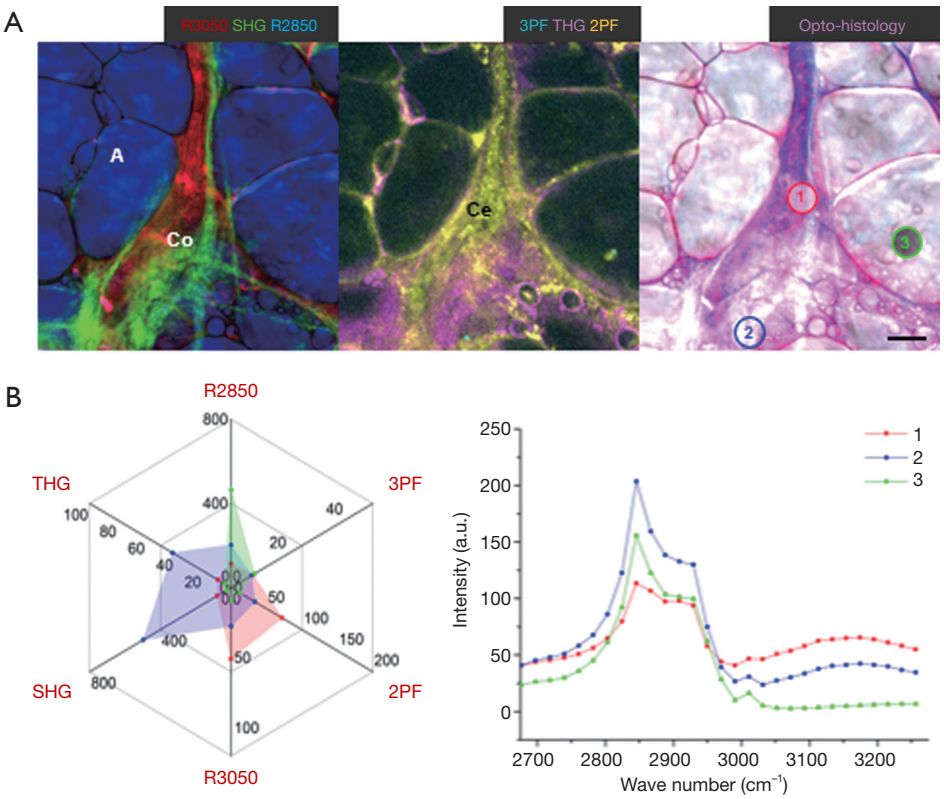

Figure 4 Multiphoton imaging and molecular profiling for normal mammary tissue showing a representative normal lipid-stroma boundary. (A) Multimodal multiphoton images and opto-histology. (B) Multiphoton molecular profiles of selected areas [1–3] indicated in the opto-histology shown in (A). Morphological features—A, adipose tissue; Ce, hypercellularity; Co, collagen fiber. Scale bar: 25 μm.

shows an MPMP similar to that of the AA3V in Area 4 at an angiogenic site. Therefore, the microvesicle in Area 3 is also likely an AA3V. An examination of the 3PF-THG-2PF image reveals few elastin fibers (2PF) and aligned AA3Vs initiating the angiogenic process between Areas 1 and 3. The histology demonstrates the stroma infiltrated with cancerous cells with dark-staining nuclei and fibrous connective tissue adjacent to the adipose tissue.

In Week 7 (not shown), the tumor developmental stage was similar to that of Week 6. Different angiogenic features were visible, such as blood vessels with high-2PF walls surrounded by AA3Vs, capillaries of similar multiphoton responses, an elastin net of crosslinking fibers, and a strand of AA3Vs. TATVs were also found confirming the tumorigenesis. Comparison of the radar plots revealed subtle differences regarding the further loss of normal tissue structure.

In Week 9, the formation of tumors 3–10 mm in size with necrotic cores were identified. Multiphoton imaging (*Figure 8*) shows a mesh-like cellular arrangement (Ne) with reduced 2PF and 3PF signals and little collagen content (SHG). A small subset of cells (Ce) shows higher 2PF. Small LDs (R2850, THG) are found exhibiting higher 2PF and 3PF. The MPMP of the small LD in Area 1 has moderate 2PF and 3PF signals, while the R2850 peak in the CARS spectrum confirms its lipid composition. Higher 2PF in Area 2 reflects some cellular metabolism, which is absent in Area 3.

Discussion

The multimodal multiphoton method offers label-free molecular imaging and molecular profiling *in situ*, in contrast to the tissue fixation, processing, sectioning, and staining required for histopathology or immunohistochemistry (26). With multimodal multiphoton imaging and molecular profiling, various breast cancer biomarkers (*Figure 3*) are identified in this longitudinal study of mammary tumor development and may serve as hallmarks for breast cancer detection and diagnosis.

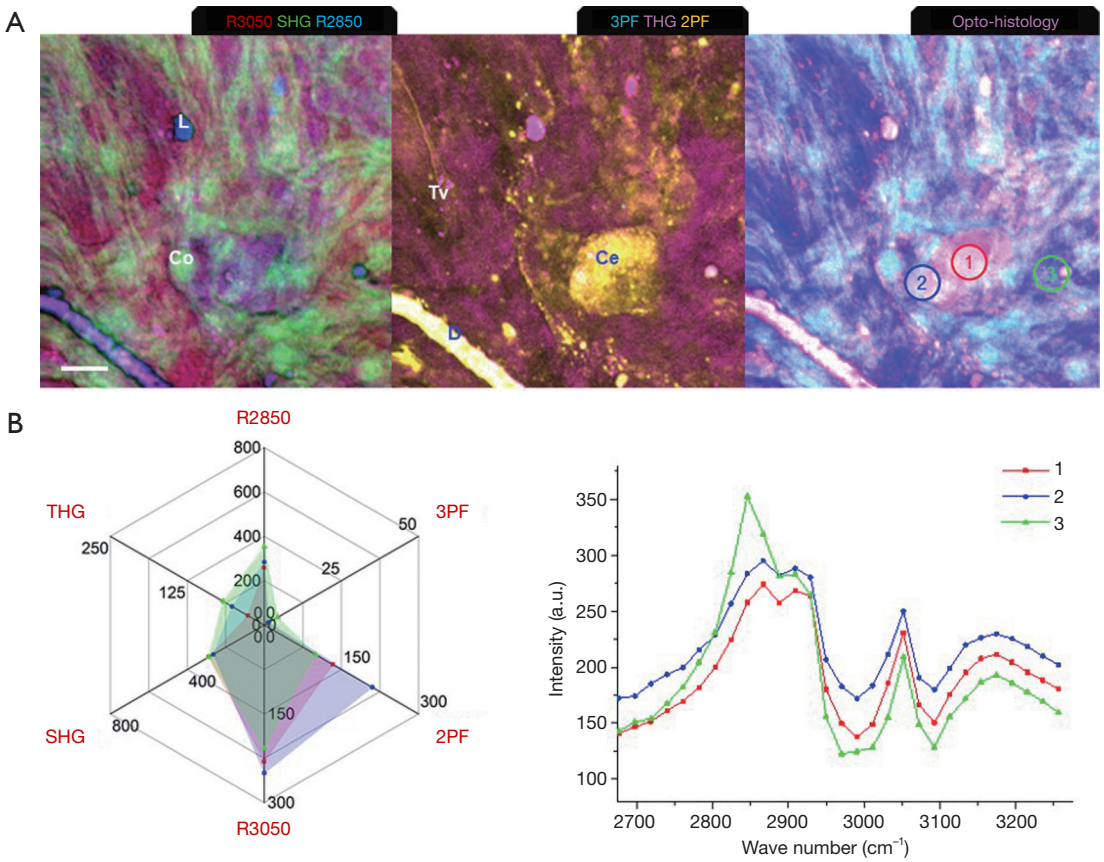

Figure 5 Multiphoton imaging and molecular profiling for mammary tumor development in Week 1, revealing the onset of hypercellularity and collagen remodeling, tumor-associated microvesicles, and lipid metabolism. (A) Multimodal multiphoton images and the opto-histology. (B) Multiphoton molecular profiles of the selected areas in the opto-histology shown in (A). Morphological features—Ce, hypercellularity; Co, collagen fiber; D, mammary duct; L, deformed lipid; Tv, THG-sensitive microvesicle. Scale bar: 25 μm.

Cellular activities are of particular importance during tumor formation (6). The cellular metabolism can be probed by fluorescence imaging of endogenous FAD and NAD(P)H, which are principal electron acceptors and donors, respectively, in the mitochondria electron-transport chain. The higher cellular FAD (*Figures 3*,*5*,*6*,*7*) and NAD(P)H fluorescence (*Figures 3A*,*8)* indicate elevated oxidative phosphorylation and anaerobic glycolysis, respectively (16-19). The co-occurrence of both FAD and NAD(P)H fluorescence and the shift from FAD to NAD(P)H fluorescence reflects the reprogramming of cellular metabolism in tumorigenesis (*Figures 3A*,*8*). In addition to metabolic imaging, the THG-sensitive cells (*Figure 3B*) imply that optical heterogeneity arose from the intracellular heterogeneity caused by tumorigenesis.

The alteration of the extracellular matrix during tumor progression can be represented by the collagen and elastin (dis)organization. The TACS features specify the collagen remodeling, including TACS-1 (*Figures 3B*,*5*) as well as TACS-2 and TACS-3 (*Figure 3A*) (15,16). Here, we propose two additional signatures: TACS-4, being indicative of locally reduced collagen (*Figure 3B*), and TACS-5 for tubularly-arranged collagen (*Figure 3A*). TACS-4 demonstrates lower SHG and shorter fibers, and may suggest the change of collagen composition from Type I to Type V (29,50). TACS-5 shows collagen fibers aligned with angiogenic features validated by 2PF and 3PF imaging. While these TACS signatures are observed by SHG and THG imaging, their biological relevance is cross-validated by multimodal multiphoton imaging, such as tumor formation, local invasion, fibrocystic tissue, and angiogenesis. The elastin organization, which contributes to tissue elasticity, is found interplaying with the collagen organization, either co-localized with or excluded from

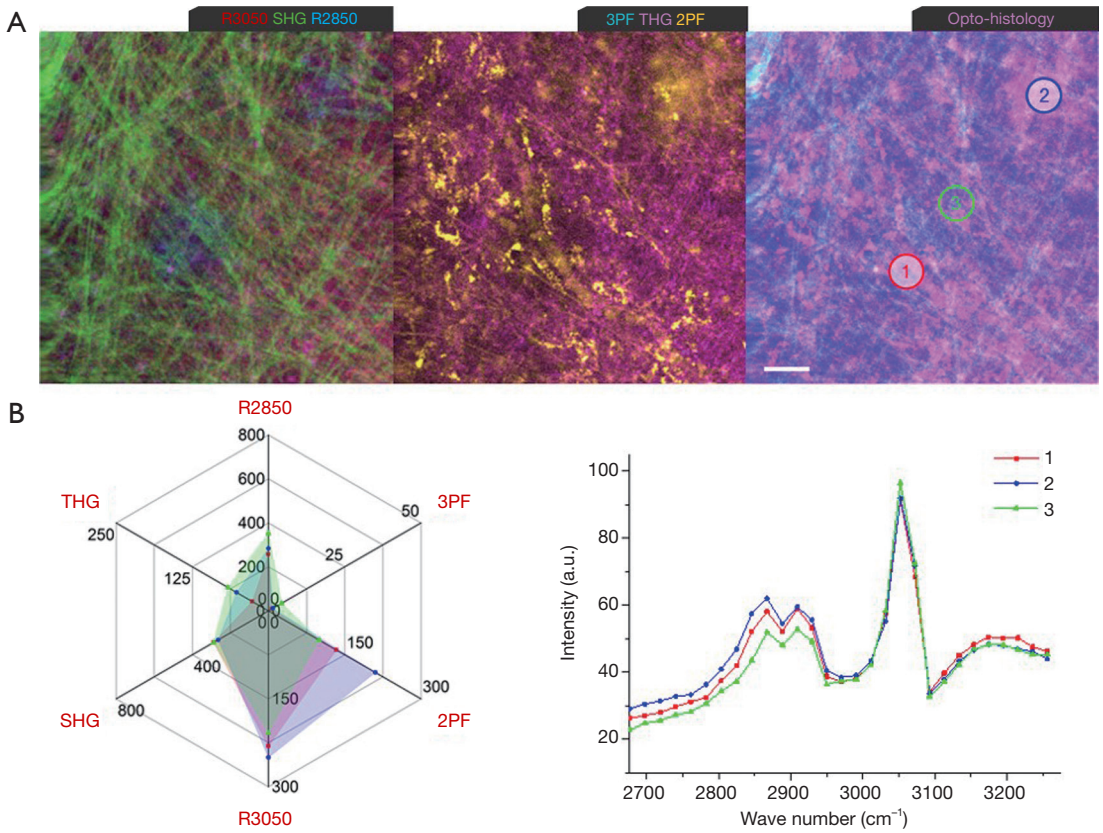

Figure 6 Multiphoton imaging and molecular profiling for mammary tumor development in Week 4, showing the formation of a tumor nest and the reduced collagen content. (A) Multimodal multiphoton images and opto-histology. (B) Multiphoton molecular profiles of the selected areas in the opto-histology shown in (A). Morphological features—Co, collagen fiber; T, tumor; Tv, THG-sensitive microvesicles. Scale bar: 25 μm.

the collagen fibers. Some elastin fibers appear in a net- or sheet-like morphology (*Figures 3*,*7*) and are likely the developing elastic lamella in neo-angiogenesis (48,49). The elastin lamella can become more tubularly aligned in the later stages of tumor progression.

The distribution of microvesicles also offers important markers for tumorigenesis (51). The TATVs are identified in various microenvironments throughout the longitudinal study (*Figures 3*,*5*,*6*,*7*), suggesting TATVs as a strong breast cancer biomarker (24,51). The MPMP analysis successfully distinguishes the TATVs from the micro-LDs by their protein-like CARS spectra and extreme THG response. By flexibly tailoring the SC pulses, multiphoton fluorescence imaging with different excitation wavelengths or CARS imaging with a broader vibrational bandwidth may help decipher the biochemical contents of the TATVs. The tubularly-aligned AA3Vs provide cues for the angiogenesis routes. Some AA3Vs are found co-existing with the elastin fibers or the vascular walls (*Figures 3*,*7*), while others appear to be associated with recruiting endothelial and tumorigenic cells (*Figure 3*). The NAD(P)H origin of the 3PF response of AA3Vs is supported by the NAD(P)H oxidase activity and the elevated NADH concentration during angiogenesis (45,46). The convoluted angiogenesis processes may be further understood by dynamic monitoring of FAD-fluorescent cells, collagen and elastin organization, as well as AA3Vs, and is of future research interest.

Lipids serve as energy reservoirs and play an important role in tumor growth and metastasis (21,22,32). Lipogenesis is recognized in the earlier stages of tumor development by the orderly accumulation of small LDs (~3–20 μm in diameter) in the stromal area with FAD-fluorescent cells and collagen fibers (*Figure 4*). Lipolysis is identified during tumor development as lipid deposits of irregular sizes and shapes formed from the degraded LDs in the stroma (*Figures 3*,*5*). In the proximity of the degraded LDs, the

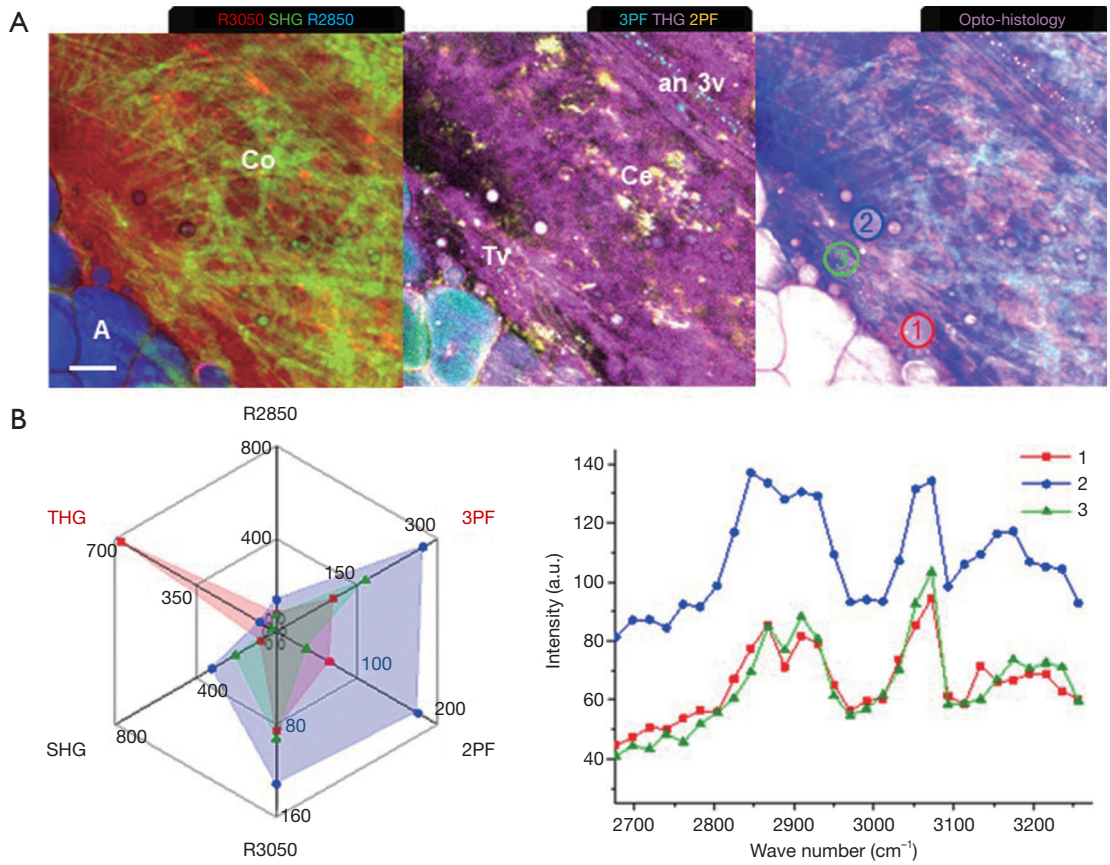

Figure 7 Multiphoton imaging and molecular profiling for mammary tumor development in Week 6, showing various tumor-associated microvesicles at a lipid-stroma interface containing tumorigenic stromal cells. (A) Multimodal multiphoton images and the opto-histology. (B) Multiphoton molecular profiles of the selected areas in the opto-histology shown in (A). Morphological features—A, adipose tissue; an, angiogenesis; Ce, hypercellularity; Co, collagen fiber; Tv, THG-sensitive microvesicle; 3v, 3PF-sensitive microvesicles. Scale bar: 25 μm.

FAD-fluorescent and NAD(P)H-fluorescent cells and amorphous features, elastin and collagen fibers, as well as AA3Vs and TATVs, are all related to diverse tumorigenic events fueled by lipid degradation (*Figures 3,5*). Multimodal multiphoton imaging interrelates the elevated FAD and NAD(P)H fluorescence and the reduced lipid content as a result of β-oxidation (47). The changes in lipid metabolism very likely affect other metabolic processes during tumor progression.

CARS microscopy is well-known to effectively map lipid and protein contents at ~R2850 and ~R2930, respectively (20-22). Nevertheless, imaging protein composition with the CH aromatic vibration at R3050 circumvents the interference from the lipid band, as in the case of R2930 (22,52,53), enabling direct visualization of increased protein content in carcinogenesis. The water molecules co-localized with the protein composition contribute to and coherently enhance the R3050 response, and offer a vibrational marker itself with a broadband response of R3200-R3400 (53). Throughout the spectra in the MPMP analysis, a prominent peak at R3050 is readily identified in the pre-cancerous and cancerous areas (*Figures 5-7*), but not in the normal tissue (*Figure 4*). However, this R3050 vibration vanishes in the sites of necrosis in Week 9 (*Figure 8*), suggesting decreased carcinogenic activity in the later stages of tumor development. Reduced activity is supported by lower cellular metabolism, reflected by low cellular FAD and NAD(P)H fluorescence in these areas (16-19). These observations establish the R3050 response as a potentially useful carcinogenic activity indicator.

Longitudinal imaging and characterization of carcinogenesis was performed in a controlled pre-clinical mammary tumor model using label-free multimodal multiphoton molecular imaging. New insights for

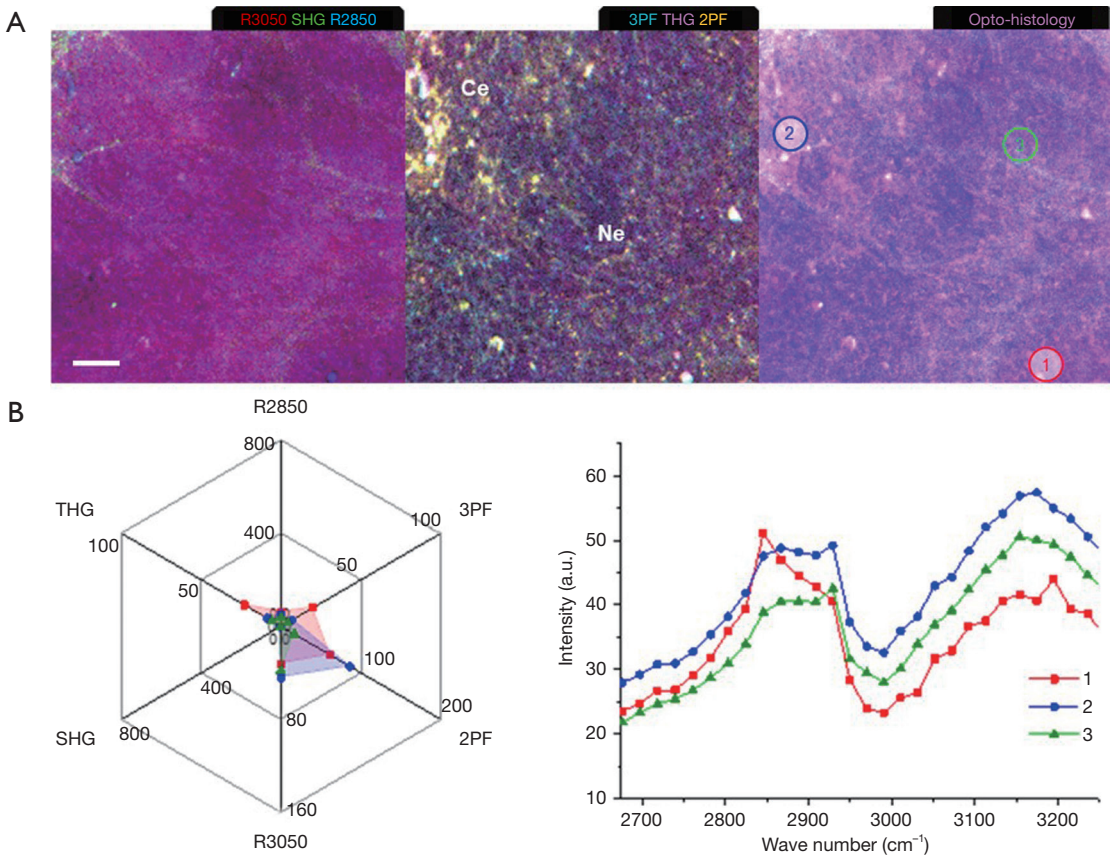

Figure 8 Multiphoton imaging and molecular profiling for mammary tumor development in Week 9, demonstrating reduced cellular metabolism and collagen contents in a necrotic core. (A) Multimodal multiphoton images and the opto-histology. (B) Multiphoton molecular profiles of the selected areas in the opto-histology shown in (A). Morphological features—Ce, hypercellularity; Ne, necrosis. Scale bar: 25 μm.

the process of carcinogenesis can be gained via penta-modal imaging and radar-plot representation, which systematically and quantitatively combines chemical, functional, and structural contrast of the authentic tumor microenvironment. The fundamentally different physical mechanisms of the different modalities provide complimentary visualization of diverse biomolecules and structures, such as FAD, collagen, NAD(P)H, lipids, proteins, and the molecular content of various microvesicles. The well-controlled SC excitation pulses offered quantitative correlation of multimodal multiphoton signals in addition to the CARS spectrum, establishing a MPMP for interrogating the biochemical composition of *in situ* microenvironments. The MPMPs in the cancerous and normal tissue reveled differences in lipid droplets, stromal tissue, and microvesicles that would otherwise be undetectable using any single modality, or by any currently available immunohistochemical or histological staining technique. These molecular characteristics are not only visualized individually, but their interaction and correlation also provide further insight into tumor invasion, cellular metabolism, angiogenesis, and lipid metabolism in the tumor microenvironment. These results demonstrate the powerful potential of this technology for molecular cancer detection and diagnosis.

Acknowledgments

We thank NKT Photonics and Biophotonic Solutions for their collaborative effort. We also thank Darold Spillman and Youbo Zhao for their technical support.
Funding: This work was supported in part by grants from the National Institutes of Health (NIH R01CA213149, SA Boppart; 1 R01 EB023232, SA Boppart).

Footnote

Conflicts of Interest: SA Boppart, H Tu, and S You are named inventors on patents filed by the University of Illinois at Urbana-Champaign related to the laser source technology and the imaging and quantification of extracellular vesicles. SA Boppart and H Tu are co-founders and hold equity interest in LiveBx, LLC, Champaign, IL, which is commercializing the laser source technology used in this study. The other authors have no conflicts of interest to declare.

Ethical Statement: The animal procedures for this study were conducted under a protocol approved by the Institutional Animal Care and Use Committee at the University of Illinois at Urbana-Champaign.

References

1. Weissleder R, Pittet MJ. Imaging in the era of molecular oncology. Nature 2008;452:580-89.
2. American Cancer Society. Cancer Facts & Figures 2015. Atlanta: American Cancer Society 2015.
3. Hosseini H, Obradovic MM, Hofmann M, Harper KL, Sosa MS, Werner-Klein M, Nanduri LK, Werno C, Ehrl C, Maneck M, Patwary N, Haunschild G, Gužvić M, Reimelt C, Grauvogl M, Eichner N, Weber F, Hartkopf AD, Taran FA, Brucker SY, Fehm T, Rack B, Buchholz S, Spang R, Meister G, Aguirre-Ghiso JA, Klein CA. Early dissemination seeds metastasis in breast cancer. Nature 2016;540:552-8.
4. Harper KL, Sosa MS, Entenberg D, Hosseini H, Cheung JF, Nobre R, Avivar-Valderas A, Nagi C, Girnius N, Davis RJ, Farias EF, Condeelis J, Klein CA, Aguirre-Ghiso JA. Mechanism of early dissemination and metastasis in Her2+ mammary cancer. Nature 2016;540:588-92.
5. Friedl P, Alexander S. Cancer invasion and the microenvironment: Plasticity and reciprocity. Cell 2011;147:992-1009.
6. Hanahan D, Weinberg RA. Hallmarks of cancer: the next generation. Cell 2011;144:646-74.
7. Yue S, Slipchenko MN, Cheng JX. Multimodal nonlinear optical microscopy. Laser Photon Rev 2011;5:496-512.
8. Denk W, Strickler JH, Webb WW. Two-photon laser scanning fluorescence microscopy. Science 1990;248:73-6.
9. Hell SW, Bahlmann K, Schrader M, Soini A, Malak HM, Gryczynski I, Lakowicz JR. Three-photon excitation in fluorescence microscopy. J Biomed Opt 1996;1:71-4.
10. Gannaway JN, Sheppard CJR. Second-harmonic imaging in the scanning optical microscope. Opt Quant Electr 1978;10:435-9.
11. Barad Y, Eisenberg H, Horowitz M, Silberberg Y. Nonlinear scanning laser microscopy by third harmonic generation. Appl Phys Lett 1997;70:922-4.
12. Zumbusch A, Holtom GR, Xie XS. Three-dimensional vibrational imaging by coherent anti-Stokes Raman scattering. Phys Rev Lett 1999;82:4142-5.
13. Freudiger CW, Min W, Saar BG, Lu S, Holtom GR, He C, Tsai JC, Kang JX, Xie XS. Label-free biomedical imaging with high sensitivity by stimulated Raman scattering microscopy. Science 2008;322:1857-61.
14. Zipfel WR, Williams RM, Christie R, Nikitin AY, Hyman BT, Webb WW. Live tissue intrinsic emission microscopy using multiphoton-excited native fluorescence and second harmonic generation. PNAS 2003;100:7075-80.
15. Provenzano PP, Eliceiri KW, Campbell JM, Inman DR, White JG, Keely PJ. Collagen reorganization at the tumor-stromal interface facilitates local invasion. BMC Med 2006;4:38.
16. Provenzano PP, Inman DR, Eliceiri KW, Knittel JG, Yan L, Ruedn CT, White JG, Keeley PJ. Collagen density promotes mammary tumor initiation and progression. BMC Med 2008;6:11.
17. Bird DK, Yan L, Vrotsos KM, Eliceiri KW, Vaughan EM, Keely PJ, White JG, Ramanujam N. Metabolic mapping of MCF10A human breast cells via multiphoton fluorescence lifetime imaging of the coenzyme NADH. Cancer Res 2005;65:8766-73.
18. Walsh A, Cook RS, Rexer B, Arteaga CL, Skala MC. Optical imaging of metabolism in HER2 overexpressing breast cancer cells. Biomed Opt Express 2012;3:75-85.
19. Ostrander JH, McMahon CM, Lem S, Millon SR, Brown JQ, Seewaldt VL, Ramanujam N. Optical redox ratio differentiates breast cancer cell lines based on estrogen receptor status. Cancer Res 2010;70:4759-66.
20. Le TT, Rehrer CW, Huff TB, Nichols MB, Camarillo IG, Cheng JX. Nonlinear optical imaging to evaluate the impact of obesity on mammary gland and tumor stroma. Mol Imaging 2007;6:205-11.
21. Le TT, Huff TB, Cheng JX. Coherent anti-Stokes Raman scattering imaging of lipids in cancer metastasis. BMC Cancer 2009;9:42.
22. Chowdary PD, Jiang Z, Chaney EJ, Benalcazar WA, Marks DL, Gruebele M, Boppart SA. Molecular histopathology by spectrally reconstructed nonlinear interferometric vibrational imaging. Cancer Res 2010;70:9562-9.

23. Débarre D, Supatto W, Pena AM, Fabre A, Tordjmann T, Combettes L, Schanne-Klein MC, Beaurepaire E. Imaging lipid bodies in cells and tissues using third-harmonic generation microscopy. Nat Methods 2006;3:47-53.
24. Weigelin B, Bakker GJ, Friedl P. Intravital third harmonic generation microscopy of collective melanoma cell invasion: principles of interface guidance and microvesicle dynamics. Intravital 2012;1:32-43.
25. Tu H, Liu Y, Turchinovich D, Marjanovic M, Lyngso JK, Laegsgaard J, Chaney EJ, Zhao Y, You S, Wilson WL, Xu B, Dantus M, Boppart SA. Stain-free histopathology by programmable supercontinuum pulses. Nat Photonics 2016;10:534-40.
26. Tu H, Liu Y, Marjanovic M, Chaney EJ, You S, Zhao Y, Boppart SA. Concurrence of extracellular vesicle enrichment and metabolic switch visualized label-free in the tumor microenvironment. Sci Adv 2017;3:e1600675.
27. You S, Tu H, Chaney EJ, Sun Y, Zhao Y, Bower AJ, Liu Y, Marjanovic M, Sinha S, Pu Y, Boppart SA. Intravital imaging by simultaneous label-free autofluorescence-multiharmonic (SLAM) microscopy. Nat Commun 2018;9:2125.
28. Sun Y, You S, Tu H, Spillman DR, Chaney EJ, Marjanovic M, Li J, Barkalifa R, Wang J, Higham AM, Luckey NN, Cradock KA, Liu ZG, Boppart SA. Intraoperative visualization of the tumor microenvironment and quantification of extracellular vesicles by label-free nonlinear imaging. Sci Adv 2018;4:eaau5603.
29. Ajeti V, Nadiarnykh O, Ponik SM, Keely PJ, Eliceiri KW, Campagnola PJ. Structural changes in mixed Col I/Col V collagen gels probed by SHG microscopy: implications for probing stromal alterations in human breast cancer. Biomed Opt Express 2011;2:2307-16.
30. Yang Y, Li F, Gao L, Wang Z, Thrall MJ, Shen SS, Wong KK, Wong ST. Differential diagnosis of breast cancer using quantitative, label-free and molecular vibrational imaging. Biomed Opt Express 2011;2:2160-74.
31. Wu X, Chen G, Lu J, Zhu W, Qui J, Chen J, Xhie S, Zhuo S, Yan J. Label-free detection of breast masses using multiphoton microscopy. PLoS One 2013;8:e65933.
32. Potcoava MC, Futia GL, Aughenbaugh J, Schlaepfer IR, Gibson EA. Raman and coherent anti-Stokes Raman scattering microscopy studies of changes in lipid content and composition in hormone-treated breast and prostate cancer cells. J Biomed Opt 2014;19:111605.
33. Liu Y, Tu H, Boppart SA. Wave-breaking-extended fiber supercontinuum generation for high compression ratio transform-limited pulse compression. Opt Lett 2012;37:2172-4.
34. Xi P, Andegeko Y, Weisel LR, Lozovoy VV, Dantus M. Greater signal, increased depth, and less photobleaching in two-photon microscopy with 10 fs pulses. Opt Comm 2008;281:1841-9.
35. Liu Y, Tu H, Benalcazar W, Chaney EJ, Boppart SA. Multimodal nonlinear imaging by pulse shaping of a fiber supercontinuum from 900 to 1160 nm. IEEE JSTQE 2012;18:1209-14.
36. Lozovoy VV, Pastirk I, Dantus M. Multiphoton intrapulse interference. IV. Ultrashort laser pulse spectral phase characterization and compensation. Opt Lett 2004;29:775-7.
37. Xu B, Gunn JM, Cruz JMD, Lozovoy VV, Dantus M. Quantitative investigation of the multiphoton intrapulse interference phase scan method for simultaneous phase measurement and compensation of femtosecond laser pulses. J Opt Soc Am B 2006;23:750-9.
38. Hellerer T, Enejder AMK, Zumbusch A. Spectral focusing: High spectral resolution spectroscopy with broad-bandwidth laser pulses. Appl Phys Lett 2004;85:25-7.
39. Arafah BM, Finegan HM, Roe J, Manni A, Pearson OH. Hormone dependency in N-nitrosomethylurea-induced rat mammary tumors. Endocrinology 1982;111:584-8.
40. Crist KA, Chaudhuri B, Shivaram S, Chaudhuri PK. Ductal carcinoma in situ in rat mammary gland. The J Surg Res 1992;52:205-8.
41. Singh M, McGinley JN, Thompson HJ. A comparison of the histopathology of premalignant and malignant mammary gland lesions induced in sexually immature rats with those occurring in the human. Lab Invest 2000;80:221-31.
42. Boppart SA, Luo W, Marks DL, Singletary KW. Optical coherence tomography: feasibility for basic research and image-guided surgery of breast cancer. Breast Cancer Res Treat 2004;84:85-97.
43. Smith AM, Mancini MC, Nie SM. Bioimaging second window for in vivo imaging. Nat Nanotechnol 2009;4:710-1.
44. Kalluri R, Zeisberg M. Fibroblasts in cancer. Nat Rev Cancer 2006;6:392-401.
45. Ushio-Fukai M. Redox signaling in angiogenesis: Role of NADPH oxidase. Cardiovasc Res 2006;71:226-35.
46. Venkateswaran A. Friedman DB, Walsh AJ, Skala MC, Sasi S, Rachakonda G, Crooks PA, Freeman ML, Sekhar KR. The novel antiangiogenic VJ115 inhibits the NADH oxidase ENOX1 and cytoskeleton-remodeling proteins. Invest New Drugs 2013;31:535-44.

47. Baenke F, Peck B, Miess H, Schulze A. Hooked on fat: the role of lipid synthesis in cancer metabolism and tumour development. Dis Model Mech 2013;6:1353-63.
48. Wang HW, Le TT, Cheng JX. Label-free imaging of arterial cells and extracellular matrix using a multimodal CARS microscope. Opt Commun 2008;281:1813-22.
49. Weis SM, Cheresh DA. Tumor angiogenesis: molecular pathways and therapeutic targets. Nat Med 2011;17:1359-70.
50. Barsky SH, Rao CN, Grotendorst GR, Liotta LA. Increased content of type-V collagen in desmoplasia of human-breast carcinoma. Am J Pathol 1982;108:276-83.
51. D'Souza-Schorey C, Clancy JW. Tumor-derived microvesicles: shedding light on novel microenvironment modulators and prospective cancer biomarkers. Gene Dev 2012;26:1287-99.
52. Meyer T, Chemnitz M, Baumgart M, Gottschall T, Pascher T, Matthaus C, Romeike BFM, Brehm BR, Limpert J, Tunnermann A, Schmitt M, Dietzek B, Popp J. Expanding multimodal microscopy by high spectral resolution coherent anti-Stokes Raman scattering imaging for clinical disease diagnostics. Anal Chem 2013;85:6703-15.
53. Surmacki J, Musial J, Kordek R, Abramczyk H. Raman imaging at biological interfaces: applications in breast cancer diagnosis. Mol Cancer 2013;12:48.

Cite this article as: Liu Y, Tu H, You S, Chaney EJ, Marjanovic M, Boppart SA. Label-free molecular profiling for identification of biomarkers in carcinogenesis using multimodal multiphoton imaging. Quant Imaging Med Surg 2019;9(5):742-756. doi: 10.21037/qims.2019.04.16

Supplementary

Table S1 Summary of the multiphoton biomarkers for breast cancer based on the individual multiphoton imaging modalities, as well as the carcinogenic events cross-validated by multiple multiphoton imaging modalities

Modality	Biomarker	Biological relevance	Reference
Signatures observed by individual modality			
2PF, 3PF	Cellular FAD fluorescence	Oxidative phosphorylation	(12,13,16,24), this study
	Increased FAD fluorescence lifetime	Metabolic shift	13
	Cellular NAD(P)H fluorescence	Aerobic glycolysis	(14-16)*, this study
	Decreased NAD(P)H fluorescence lifetime	Metabolic shift	(14)
	Increased redox ratio	Metabolic shift	(15,16)*
	Elastin organization	Elastic lamella synthesis in angiogenesis, fibrocystic tissue	(34)#, this study
	Angiogenesis-associated 3PF-sensitive microvesicle (AA3V)	Upregulated NAD(P)H in angiogenesis	This study
SHG	Collagen organization (also observed by THG): TACS-1: locally dense collagen; TACS-2: straightened collagen tumor boundary; TACS-3: radially aligned collagen to TACS-2; TACS-4: locally reduced collagen; TACS-5: tubularly aligned collagen	Small tumorigenic region; increased tumor volume; invasive and metastatic growth; disruption and degradation of connective tissue; collagen enclosure in angiogenesis	(12,13,22), this study
THG	Tumor-associated THG-sensitive microvesicle (TATV)	Carcinogenesis, signaling molecule	(21)#, this study
	Stellate structure (also observed by CARS)	Lipid degradation, lipolysis	This study
	THG-sensitive cell	Intracellular heterogeneity	This study
	Disrupted axon fiber (also observed by CARS)	Caused by other tumorigenic events	This study
	Small lipid droplet, lipid vesicle (also observed by CARS)	Signaling lipid vesicle, lipid metabolism	This study
CARS, SRS	Regulated lipid composition (CH_2 stretching): increased lipid content; decreased lipid content; deformed lipid deposit; increased cholesterol content	Excessive lipid, lipogenesis; lipid degradation, lipolysis; lipid degradation, lipolysis; carcinogenesis, increased hormone level	(17-19,25,47)#, this study
	Increased protein content (CH aromatic stretching, CH_3 stretching)	Carcinogenesis	(19,39)*, this study
	Water content (OH stretching)	Water co-localized with protein	(39)*, this study
	Mammary duct (also observed by 2PF, 3PF, THG)	Mammary duct formation	(23), this study
Events revealed by multiple modalities			
2PF, SHG, 3PF, THG, CARS	Cellular FAD fluorescence; elastin organization; TACS-1,2,3,4,5; cellular NAD(P)H fluorescence; AA3V; TATV; decreased lipid content (CH_2 stretching); increased protein content (CH aromatic stretching); water content (OH stretching)	Local invasion	(12,13,21)#, this study
2PF, SHG, THG	Cellular FAD fluorescence; elastin organization; TACS-1	Fibrocystic tissue	(24), this study
2PF, SHG, 3PF, CARS	Cellular FAD fluorescence; elastin organization; TACS-4,5; AA3V; increased lipid content (CH_2 stretching)	Angiogenesis	(34)#, this study
2PF, SHG, THG, CARS	Cellular FAD fluorescence; elastin organization; TACS-1; TATV; increased lipid content (CH_2 stretching); increased protein content (CH aromatic stretching)	Lipogenesis	(17,18), this study
2PF, 3PF, THG, CARS	FAD fluorescent lipid; NAD(P)H fluorescent lipid; TACS-4; decreased lipid content (CH_2 stretching); increased protein content (CH aromatic stretching); water content (OH stretching)	Lipolysis, β-oxidation	This study
SHG, CARS	High SHG response; lipid content (CH_2 stretching)	Cholesterol crystallization	(48)#, this study

*, non-multiphoton; #, non-breast cancer.

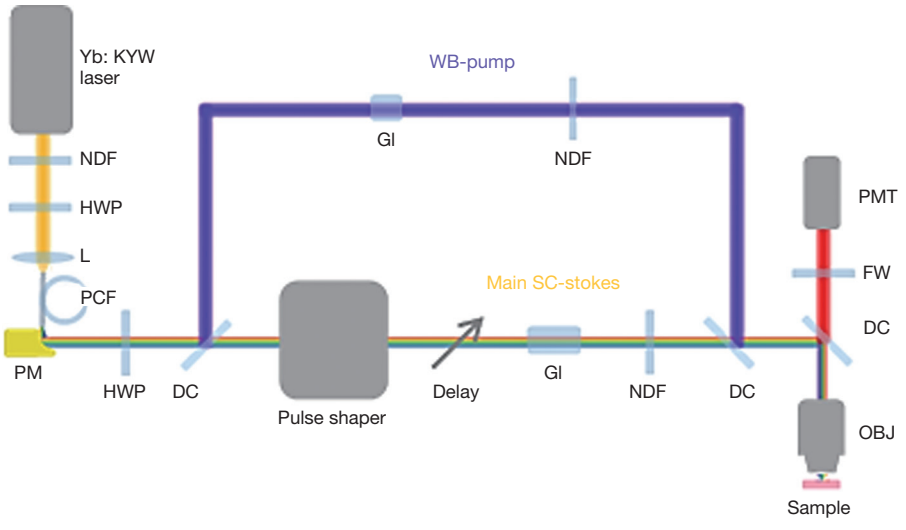

Figure S1 Schematic of the imaging system. DC, dichroic mirror; FW, filter wheel; Gl, glass; HWP, half-wave plate; KYW, potassium yttrium tungstate; L, lens; NDF, neutral density filter; OBJ, objective; PCF, photonic crystal fiber; PM, parabolic mirror; PMT, photomultiplier tube; Yb, ytterbium.

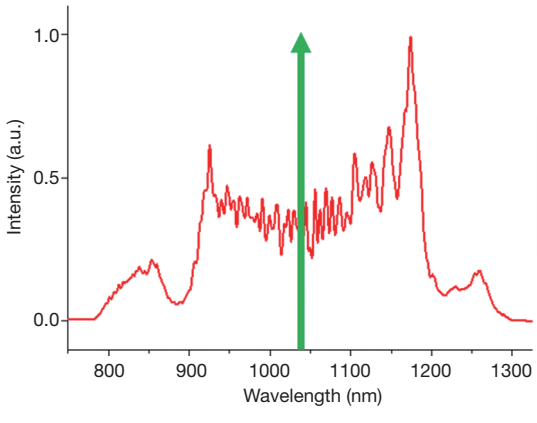

Figure S2 Spectrum of the coherent supercontinuum. Green arrow indicates the pump laser wavelength.

Table S2 Parameters for multimodal multiphoton imaging. Selected excitation and detection spectral ranges for multimodal multiphoton imaging, the pulse shapes, targeted biomolecules and structures, and optical powers under the microscope objective

Modality	Excitation wavelength (nm)	Pulse shape	Detection wavelength (nm)	Targeted biomolecule & structure	Optical power under objective (mW)
2PF	910–970	Transform-limited	542–582	FAD, elastin	5.5
SHG	1,140–1,200	Transform-limited	571–600	Collagen	10.0
3PF	1,140–1,200 (week 1–5), 1,080–1,200 (week 6–9)	Transform-limited	417–477	NAD(P)H	16.6
THG	1,140–1,200	Transform-limited	381–399	Microvesicles, lipid, nerve, collagen	10.4
CARS	780–880 (pump), 1,030–1,215 (stokes)	Optimally chirped	642–705	Lipid, protein, water	11.1 (pump), 21.0 (Stokes)